GSA Data Repository 2019251

Granular zircon from Vredefort granophyre (South Africa) confirms the deep injection model for impact melt in large impact structures

Elizaveta Kovaleva[1], Dmitry A. Zamyatin[2,3], and Gerlinde Habler[4]

[1] *Department of Geology, University of the Free State, 9300 Bloemfontein, South Africa;*

kovalevae@ufs.ac.za

[2] *Zavaritsky Institute of Geology and Geochemistry, Ural Branch of Russian Academy of Sciences, 620016 Ekaterinburg, Russia; zamyatin@igg.uran.ru*

[3] *Institute of Physics and Technology, Ural Federal University, 620002 Ekaterinburg, Russia*

[4] *Department of Lithospheric Research, University of Vienna, 1090 Vienna, Austria;*

gerlinde.habler@univie.ac.at

Item DR1. METHODOLOGY

Optical and Scanning Electron Microscopy (SEM) and cathodoluminescence (CL) imaging

Petrographic polished thin sections were prepared and analyzed with the optical microscope Olympus BX51 equipped with the camera Olympus U-TVO.63XC at the Geology Department, University of the Free State, South Africa. Subsequently thin sections were inspected with the Jeol JSM-6610 SEM equipped with an energy-dispersive X-ray (EDX) spectrometer at the same Department. The EDX detector was used to qualitatively identify mineral phases. The backscattered electron (BSE) images and qualitative chemical maps were collected at electron beam conditions of 15 KV accelerating voltage and 8 nA probe current

at 10 mm working distance, and at 9.6x10-5 Pa chamber vacuum. Panchromatic CL images were obtained using the electron probe microanalyser Cameca SX100, at the Laboratory of physical and chemical research methods, Zavaritsky Institute of Geology and Geochemistry Ural Branch of Russian Academy of Sciences, Russia.

Raman Spectroscopy

Raman spectra were obtained using a Horiba LabRAM HR800 Evolution spectrometer at the Laboratory of physical and chemical research methods, Zavaritsky Institute of Geology and Geochemistry Ural Branch of Russian Academy of Sciences, Russia. The dispersive system was equipped with an Olympus BX series optical microscope and a Peltier-cooled charge-coupled device (CCD) detector. He-Ne 632.8 nm excitation (10 mW at the sample surface) and diffraction grating with 600 grooves/mm in the optical pathway were used. An Olympus 100x objective (numerical aperture 0.9) was used to focus the laser beam onto the sample surface. The system was operated in confocal mode, resulting in a lateral resolution of ~1 μm and depth resolution ~3 μm. Hyperspectral Raman maps were obtained using a software-controlled x-y sample stage and color-coded maps were produced using Horiba's Labspec v. 6.4.4.16 software. Raman spectra for the analyzed spots were extracted from hyperspectral Raman maps. The intensity ratios of intensive zircon bands B1g (peak with position 1008 cm-1 in well-crystalline pure zircon) and Eg (peak with position 356 cm-1 in well-crystalline pure zircon) were measured after the background correction. The bands fitting was done assuming Gaussian-Lorentzian band profiles. Measured bandwidths (full width at half band-maximum; FWHM) were corrected for the apparatus function employing the empirical formula of Váczi (2014). The data were processed and plotted with the LabSpec and Excel software.

Electron Probe Microanalyses (EPMA)

The electron probe microanalysys of the chemical composition in analytical points were performed using the Cameca SX100 EPMA at the Laboratory of physical and chemical research methods, Zavaritsky Institute of Geology and Geochemistry UB of RAS. To measure the concentrations of U and Th with high accuracy, accelerating voltage 15 kV and current 200 nA were used. The concentrations of U and Th were standardized by the analytical X-ray lines of U Mβ and Th Mα on the LPET and PET (2d = 8.75Å) crystals, respectively. The intensity of the U Mβ, Th Mα and Pb Mα lines at maximum were measured for 380, 330 and 360 seconds, respectively; the lines Mg Kα, Al Kα, Si Kβ, P Kα, S Kα, K Kα, Ca Kα, Ti Kα, Mn Kα and Fe Kα were measured for 10-20 seconds; Y Lα, Zr Lβ, Tb Lα, Dy Lα, Ho Lα, Er Lα, Tm Mα, Yb Mα, Lu Mα and Hf Mα were measured for 30-100 seconds. Background intensity was determined for a half time for both sides of the maximum. During the measurements of element concentrations, interference of the Th Mγ line on U Mβ and Th Mξ lines; Y Lγ2,3 line on Pb Mα and Zr Lα lines; Ca Kβ(2) line on P Kα line; Tb Lβ4 line on Er Lα line; Mn Kβ line on Dy Lα line; Al Kα line on Tm Mα line; Lu Mβ line on Hf Mα; and U Mα(2) line on Lu Mα line was accounted for. The achieved detection limits of minor and trace elements Mg, Al, P, S, K, Ca, Ti, Mn, Fe, Y, Tb, Dy, Ho, Er, Tm, Yb, Lu, Hf, U, Th and Pb were below 88, 71, 93, 122, 88, 97, 265, 380, 362, 206, 354, 540, 395, 380, 186, 200, 182, 143, 182, 102 and 80 ppm, respectively. Calibration standards used are well-characterized natural and synthetic materials. Highly homogeneous zircon M1 from the Mir kimberlite pipe, which has a constant stoichiometric chemical composition and low Hf content (0.89 wt%) throughout the entire crystal, was used to calibrate Zr and Si. Magnesium oxide was used to calibrate for Mg, diopside was used to calibrate for Ca, apatite - for P, aluminium oxide - for Al, orthoclase - for K, rutile - for Ti, rhodonite – for Mn, hematite - for

Fe, CuFeS2 - for S, aluminum silicate glass samples doped with rare earth elements were used to calibrate for Y, Tb, Dy, Ho, Er, Tm, Yb and Lu, UO2 – for U, ThO2 – for Th, PbS – for Pb and metallic Hf – for Hf. The correction of the composition was implemented using the PAP method (Pouchou and Pichoir 1984). Low totals for the EPMA analyses, presented in the Supplemental Table 1, are explained by porous texture of the zircon grain (e.g. see Supplemental Figure 01), which causes decreased analyzed volume in the data points. Radiation doses were calculated using measured U and Th concentrations in accordance with Murakami et al. (1991).

The microprobe maps were collected under the accelerating voltage 15 kV and current 200 nA with pixel size of 0.2 μm. Maps were plotted in PeakSight v4 software at maximum intensity of lines U Mβ, Th Mα, Hf Mα (in counts), which value is proportional to the element concentrations. To avoid increasing signal noise and time expenditure, backgrounds of these lines were not recorded neither subtracted.

Electron Backscatter Diffraction (EBSD) Analyses

Deformation microstructures and textures of zircon were analyzed by orientation contrast images collected with a forescatter electron (FSE) detector, and analyzed in situ by crystallographic orientation mapping based on electron backscattered diffraction (EBSD) in a field-emission gun scanning electron microscope (FEG-SEM). FSE imaging and EBSD analyses were performed at the Laboratory for scanning electron microscopy and focused ion beam applications, Faculty of Earth Sciences, Geography and Astronomy, University of Vienna, Austria.

The thin section sample was chemo-mechanically polished using the Struers OP-S suspension of colloidal silica, and a Logitech CP50 rotary-head polishing machine. The polished sample

was coated with a thin (single thread evaporation) carbon layer in a Leica SCD500 Sputter-Coater. Orientation contrast images were taken with an FSE detector mounted on the EBSD-tube of an FEI Quanta 3D FEG instrument, which is equipped with a Schottky field emission electron source, an EDAX Pegasus Apex 4 system consisting of a Digiview IV EBSD camera and an Apollo XV silicon drift detector for EDX analysis. Electron beam conditions for analyses were at 15 kV accelerating voltage, 4 nA probe current using the analytic mode. Stage settings were at 70° tilt and 14 mm working distance. First, potentially deformed crystals were identified based on FSE images at c. 7 mm retracted EBSD tube to maximize orientation contrast. Subsequently, EBSD crystallographic orientation mapping was applied to selected zircon crystals at full insertion position of the EBSD tube. An EBSD camera binning of 4 × 4 was used to index single frame data at 49 ms exposure time, reaching indexing rates of c. 20 points per second. The Kikuchi pattern contrast was improved by applying both static and dynamic background subtraction filters and intensity histogram normalization. Hough transformation settings were at 120x120 pixels binned pattern size and 1° Theta step size, while the Rho fraction was limited to the inner 88% of the Kikuchi pattern. A 9x9 convolution mask was applied to index 3 – 15 peaks with a minimum peak distance of 8 pixels in Hough space. The interplanar angle tolerance for indexing identified bands was set to 2°. The following lattice parameters were used for reference: Zircon, di-tetragonal, Laue group 4/mmm, a=b=6.612 Å, c=5.983 Å, □=□=□=90° (Finch et al., 2001). Map data were collected in hexagonal grid mode using a step size of 70 or 80 nm. EDX intensities and EBSD data were collected simultaneously using the EDAX OIM v7.3 Data Collection software. The EBSD data were re-indexed, plotted and analyzed with the EDAX OIM v7.3 Analysis software. Data re-indexing was assisted by assigning data points to zircon based on selected EDX intensity ranges in certain EDX energy regions of interest. Crystallographic orientation maps were cleaned using the Confidence Index (CI)

Standardization procedure (CI>0.1), which unifies the confidence index of equally oriented points within a grain (presuming a minimum grain size of 3 pixels in more than one row, and a misorientation tolerance angle of 5°). The Confidence Index represents the difference in the number of triangles (found between three bands each) between the first and second orientation solution, divided by the total number of identified triangles. There was no orientation data changed during cleanup.

References

Finch, R.J, Hanchar, J.M., Hoskin, P.W.O., and Burns, P.C., 2001, Rare-earth elements in synthetic zircon: Part 2. A single-crystal X-ray study of xenotime substitution: American Mineralogist, v. 86, p. 681-689.

Murakami, T., Chakoumakos, B.C., Lumpkin, G.R., Weber, W.J., 1991. Alpha-decay event damage in zircon. American Mineralogist 76:1510-1532.

Pouchou, J.L., Pichoir, F., 1984, A new model for quantitative X-ray micro-analysis, Part I: Application to the analysis of homogeneous samples: La Recherche Aerospatiale, v. 3, p. 13–38.

Váczi, T., 2014. A new, simple approximation for the deconvolution of instrumental broadening in spectroscopic band profiles: Applied Spectroscopy, v. 68, Iss. 11, p. 1274–1278.
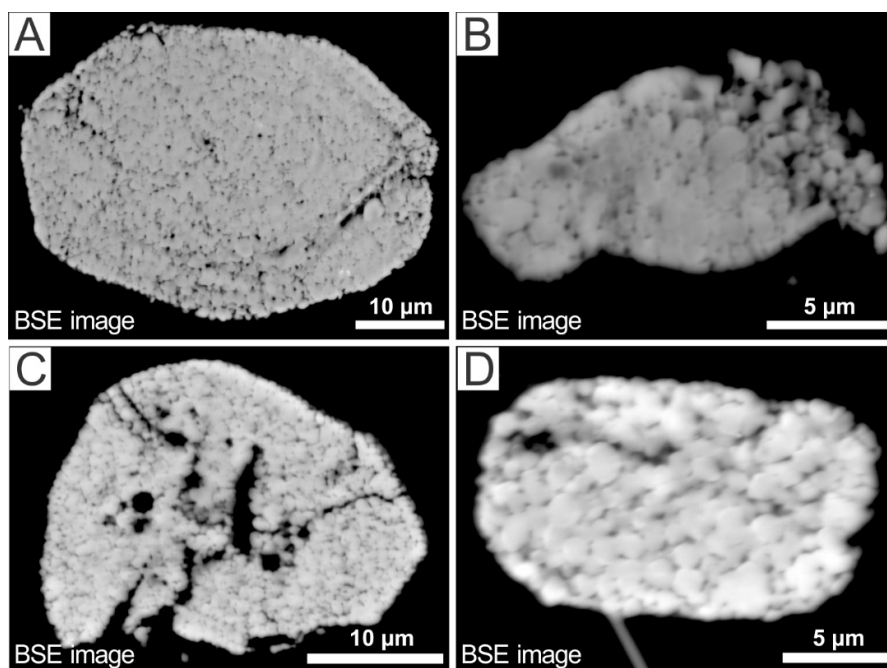
Figure DR1. BSE images of granular zircon. **(A)** Zircon aggregate at ~1.5 mm from the pseudotachylite vein; showing characteristic porosity, granular microstructure and weak concentric z-contrast zoning. This zircon has been further analyzed by CL imaging, EPMA, EBSD analysis and Raman spectroscopy. **(B)** and **(C)** Zircon aggregates at ~2 mm from the vein. **(D)** Zircon aggregate within the vein.
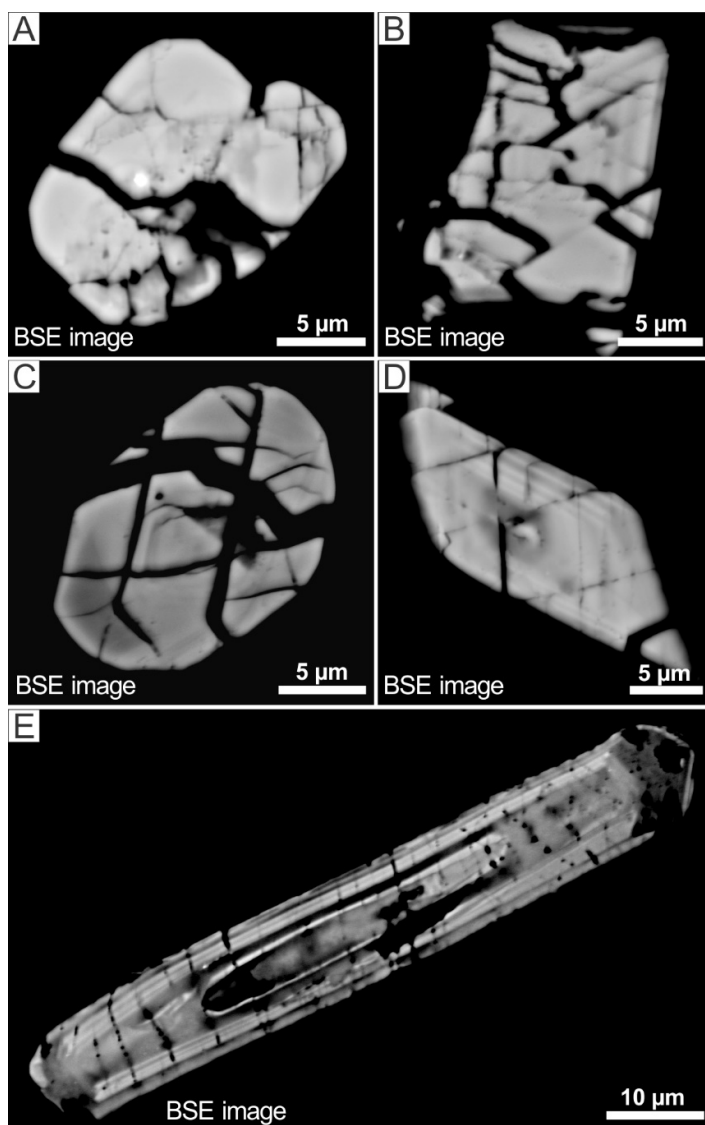
Figure DR2. BSE images of zircon with planar and curviplanar fractures. **(A)** 2.5 mm from the vein. **(B)** 7 mm from the vein. This grain was partially recrystallized to FRIGN texture its upper left portion. **(C)** 7.7 mm from the vein. **(D)** 11 mm from the vein. **(E)** 9 mm from the vein.
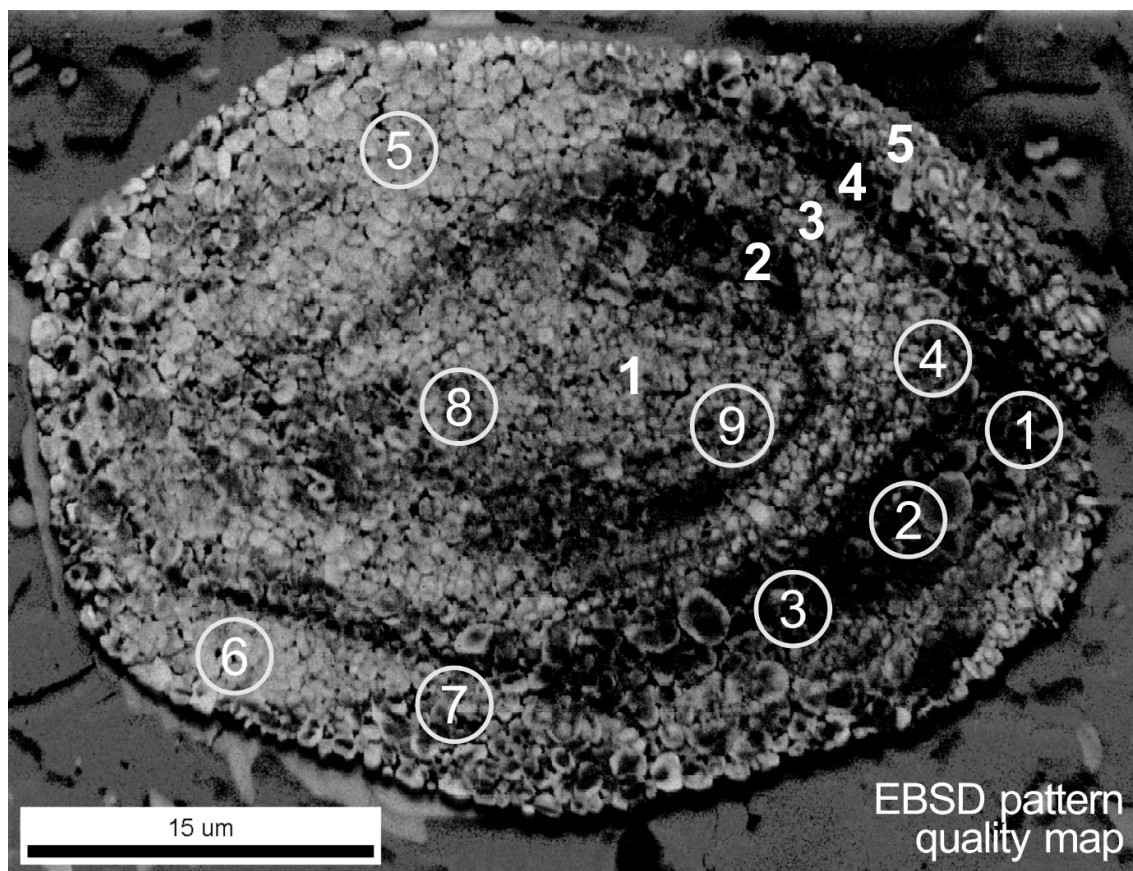
Figure DR3. EBSD pattern quality map with circles showing the positions wherefrom EPMA data have been collected (Supplemental Table 1, RD5). Numbers 1-5 (without circles) mark the described growth zones (1 – inner core, 2 – outer core, 3 – mantle, 4 – inner rim, 5 – outer rim).

Table DR 1. Chemical compositions (in oxides wt.%) of zircon Clast01-03 as determined by EPMA analysis. The positions of the analyzed spots are marked in the Supplemental Figure 4 (DR6). The very narrow outer core (zone 2) was not analyzed. Point 7 (outer rim) has elevated UO2 and probably represents a mixed analysis of the outer and inner rim (DR6).

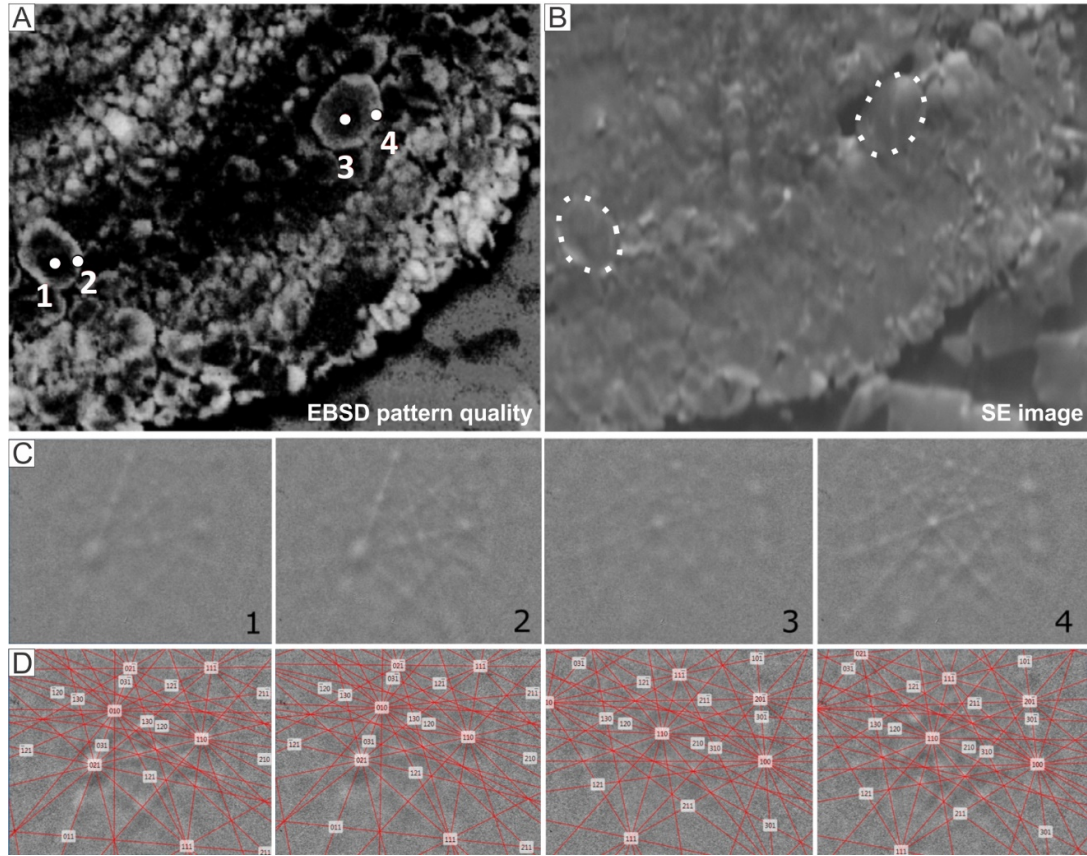|	Standard: Zircon M1	1	2	3	4 Mantle (zone 3)	5	6	7 Mixture (outer + inner rim)	8	9
		Inner rim (zone 4)				Outer rim (zone 5)			Inner core (zone 1)	
MgO	[*]bdl	0.06	0.06	0.03	0.03	bdl	0.31	1.81	0.02	0.02
Al_2O_3	bdl	2.71	0.55	0.27	0.12	0.07	0.52	3.12	0.07	0.09
SiO_2	32.68	33.76	31.45	32.54	32.51	32.95	33.08	32.96	33.50	33.92
P_2O_5	bdl	0.56	0.46	0.49	0.11	0.04	0.03	0.07	0.10	0.13
SO_2	bdl	bdl	0.03	0.02	0.03	0.03	0.03	0.03	bdl	bdl
K_2O	bdl	0.12	0.02	0.02	bdl	bdl	0.16	0.55	bdl	bdl
CaO	bdl	0.60	0.75	0.85	0.05	0.02	0.04	0.04	bdl	0.02
TiO_2	bdl	bdl	bdl	bdl	bdl	bdl	bdl	0.10	bdl	bdl
MnO	bdl	0.04	0.06	bdl	bdl	bdl	bdl	bdl	bdl	bdl
FeO	bdl	0.47	0.39	0.28	0.12	0.09	0.51	2.52	0.05	0.09
Y_2O_3	bdl	0.48	0.81	0.41	0.08	0.04	0.06	0.09	0.15	0.13
ZrO_2	66.08	54.17	60.87	59.94	64.33	63.40	62.77	55.77	62.86	62.13
Tb_2O_3	bdl	bdl	bdl	bdl	bdl	bdl	bdl	bdl	bdl	bdl
Dy_2O_3	bdl	0.03	0.04	0.03	bdl	0.00	bdl	bdl	bdl	bdl
Ho_2O_3	bdl	bdl	0.05	bdl	bdl	bdl	bdl	bdl	bdl	bdl
Er_2O_3	bdl	0.06	0.09	0.08	bdl	bdl	bdl	0.04	bdl	bdl
Tm_2O_3	bdl	0.03	0.03	0.03	bdl	bdl	bdl	0.01	bdl	0.02
Yb_2O_3	bdl	0.08	0.09	0.08	bdl	bdl	bdl	bdl	bdl	bdl
Lu_2O_3	bdl	bdl	bdl	bdl	bdl	bdl	bdl	bdl	bdl	bdl
HfO_2	1.05	0.96	1.02	0.95	1.07	1.25	1.26	1.14	1.05	0.97
PbO	bdl	0.03	0.04	0.04	0.01	bdl	bdl	bdl	0.01	0.01
ThO_2	bdl	0.10	0.11	0.13	0.03	0.02	bdl	0.03	0.03	0.03
UO_2	bdl	0.17	0.15	0.17	0.05	0.03	0.08	0.20	0.04	0.05
Total	99.81	94.45	97.05	96.36	98.52	97.94	98.87	98.48	97.89	97.61

[*] bdl = below detection limit.

Figure DR4. Analysis of crystal orientation and degree of crystallinity in zones within individual neoblasts. **A.** Detail of EBSD pattern quality map in Fig 1 (main text). White dots indicate the locations wherefrom the Kikuchi pattern shown in (C)-(D) have been generated. **B.** Secondary electron image of the same area as in (A), analyzed grains are outlined with the white dotted lines. **C.** and **D.** Kikuchi patterns from points 1-4, marked in (A). The crystallographic orientations at points 1-2 and 3-4 are the same (D), but the pattern quality (pattern contrast and band sharpness) is significantly poorer in points 1 and 3 than in 2 and 4 accordingly. EBSD indexing shows that the mean angular deviation value in the cores of neoblasts is systematically 20-50% higher than in the rims.
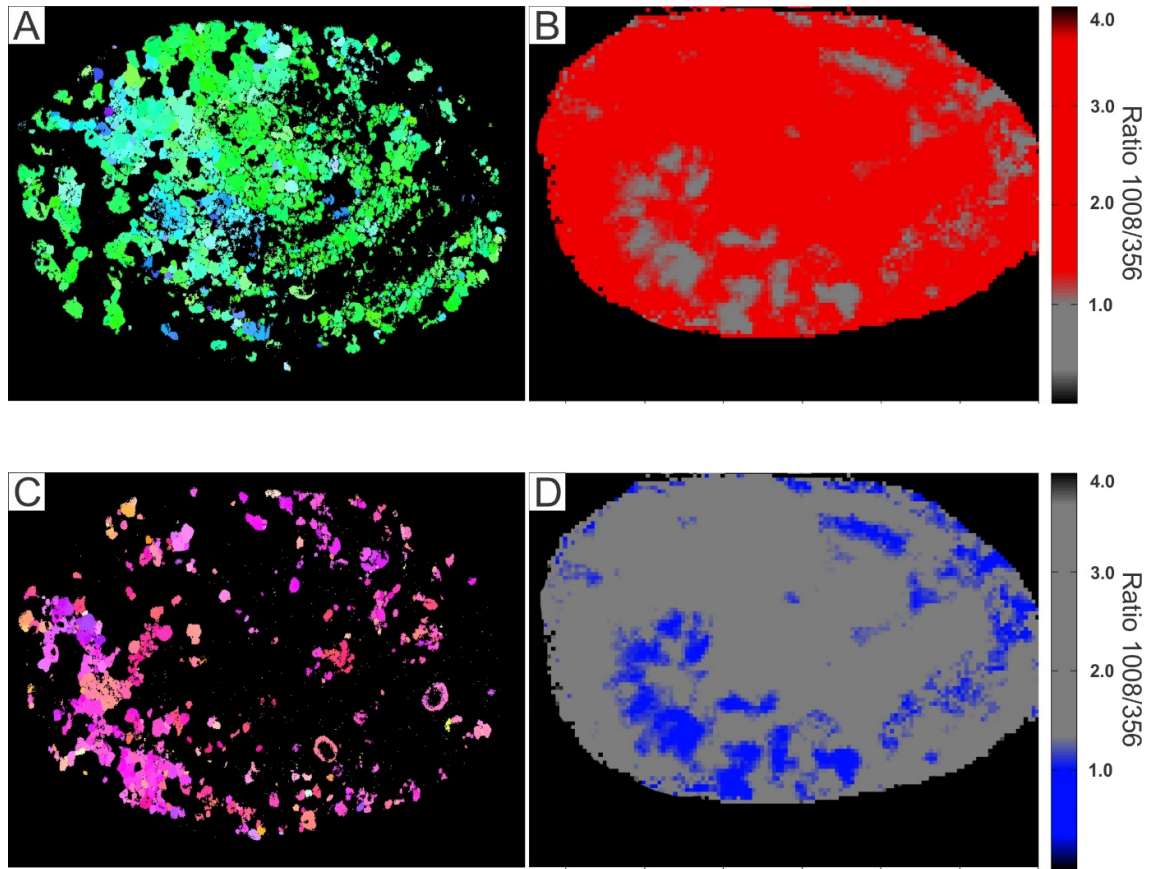
Figure DR5. Spatial comparison of the domains between the EBSD map in inverse pole figure colors and the Raman B_{1g}/E_g band intensity ratio map. **A.** Cumulative misorientation EBSD map, first orientation cluster is highlighted with blue-green color scheme; misorientation of Zrn[001] from blue to green is 25°. **B.** Raman B_{1g}/E_g band intensity ratio map (see Fig. 3F in the main text), only pixels with the ratio above 1.0 are highlighted (red). Highlighted domains in A and B roughly coincide. **C.** Cumulative misorientation EBSD map, second orientation cluster is highlighted with pink-yellow color scheme; misorientation of Zrn[001] from pink to yellow is 25°. **D.** Raman B_{1g}/E_g band intensity ratio map, only pixels with the ratio below 1.0 are highlighted (blue). Highlighted domains in C and D roughly coincide. The coincidence is not exact, because of the different spatial resolution and penetration depth of the two compared techniques.
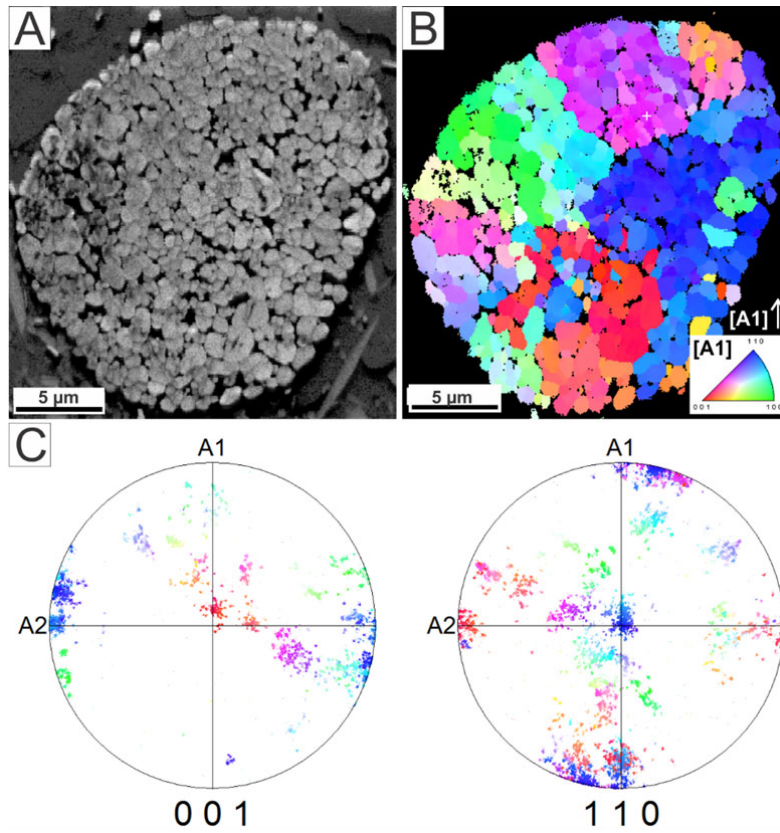
Figure DR6. EBSD crystal orientation data of granular neoblastic zircon within the pseudotachylite vein. **A.** EBSD pattern quality map showing increased pore size compared to granular zircon in granite host, indicative of resorption of neoblasts within the pseudotachylite matrix. **B.** EBSD inverse pole figure map using the thin section normal as reference direction. **C.** Equal angle lower hemisphere projection pole figures, showing directions of crystallographic zircon axes [001] and <110>. Color-coding as in (B). Red and dark blue-colored domains have orthogonal orientation relationship (likely the remnant FRIGN signature), whereas other aggregate domains show unsystematic orientation variations. This suggests that the FRIGN signature of this zircon aggregate might have been disturbed, or that there was not reidite present in this grain.